3D printed scaffolds with controlled micro-/nano-porous surface topography direct chondrogenic and osteogenic differentiation of mesenchymal stem cells

Aruna Prasopthum[†], Mick Cooper[§], Kevin M Shakesheff[†], Jing Yang[†],*

[†]Division of Regenerative Medicine and Cellular Therapies, School of Pharmacy, University of Nottingham, Nottingham, NG7 2RD, UK

[§]School of Chemistry, University of Nottingham, Nottingham, NG7 2RD, UK

KEYWORDS: 3D printing, scaffolds, micro-/nano-pores, stem cells, differentiation

ABSTRACT

The effect of topography in 3D printed polymer scaffolds on stem cell differentiation is a significantly under-explored area. Compared to 2D biomaterials on which various well-defined topographies have been incorporated and been shown to direct an arrange of cell behaviours including adhesion, cytoskeleton organisation and differentiation, incorporating topographical features to 3D polymer scaffolds is challenging due to the difficulty of accessing the inside of a porous scaffold. Only roughened strut surface has been introduced to 3D printed porous

scaffolds. Here, a rapid, single-step 3D printing method to fabricate polymeric scaffolds consisting of micro-struts (ca. 60 µm) with micro-/nano-surface pores (0.2-2.4 µm) has been developed based on direct ink writing of an agitated viscous polymer solution. The density, size, and alignment of these pores can be controlled by changing the degree of agitation or the speed of printing. 3D printed scaffolds with micro-/nano-porous struts enhanced chondrogenic and osteogenic differentiation of MSCs without soluble differentiation factors. The topography also selectively affected adhesion, morphology and differentiation of MSC to chondrogenic and osteogenic lineages depending on the composition of the differentiation medium. This fabrication method can potentially be used for a wide range of polymers where desirable architecture and topography are required.

INTRODUCTION

One goal of tissue engineering is to develop bio-instructive scaffolds that not only provide a temporary matrix to accommodate cells, but also direct adhesion, migration, proliferation and differentiation of stem cells to the desired lineage.[1] Mesenchymal stem cells (MSCs) are an important cell source in tissue engineering due to their ability to self-renew, proliferate and differentiate into a wide range of tissue-specific lineages, including chondrogenic and osteogenic/osteoblastic lineages, which can be directed by appropriate biomaterial physical or chemical cues.[2–4]

Cells in their natural 3D environment experience various micro- to nano-scale topographies of the hierarchical structures of extracellular matrix (ECM), which play a vital role in modulating cell behaviour.[5] The flattened elliptical chondrocytes in the superficial zone of articular cartilage, for instance, reside within a network of parallelly organised collagen type II fibrils with 20-

2

30 nm diameters for resisting high shear and tensile forces[6]. Stellate-shaped osteocytes in bone tissue are surrounded by a gel-like pericellular proteoglycan matrix with a fibre spacing of approximately 7 nm within lacunae.[7] The advances in micro- and nano-scale fabrication techniques such as lithography have enabled the investigation of cell- micro-/nano-topography interactions onto 2D substrates with well-defined isotropic (evenly or randomly distributed pits, protrusions, pillar) or anisotropic (ridges or grooves) surfaces.[8–14] For example, the combination of micro- and nano-grooves in parallel or perpendicular directions have been used to demonstrate the synergistic or competitive effects between micro- and nano-topographies on MSC spreading[8]. Pits with different microscale sizes (diameter of 20, 30 and 40 μm)[13] and pits with the same nanoscale size (diameter of 200 nm) but different distribution patterns (e.g., square array, hexagonal array, disordered square) have been shown to differently affect cytoskeleton organisation, osteogenic differentiation[14], or multipotency of MSCs in long-term culture.[12] Overall, it has been well established that fate commitment of MSCs towards osteogenic lineage can be regulated directly by topography via actin cytoskeleton-integrin generated tension during cell adhesion, which is transmitted to the nucleus by intracellular signalling pathways triggered by key mediators including focal adhesion kinase (FAK) and integrin linked kinase (ILK).[11,12,15–17] However, the study on how topographies regulate chondrogenesis of MSCs is limited. Only a few studies have shown the direct effect of the polymer material surfaces on cell morphology and chondrogenic differentiation of MSCs. Indeed, enhancement in the expression of chondrogenic gene markers was observed if micro-patterned 2D substrates could prevent spreading and flattening of MSCs[18–20] or when actin cytoskeleton was chemically disrupted.[21] However, almost all reports on MSC-topography interactions have been based on 2D systems.

It has been well recognised that cells behave differently in 3D compared to 2D. For instance, a recent study has shown markedly higher osteogenic differentiation capability of adipose tissue-derived MSCs cultured in 3D printed scaffolds than those on 2D substrates.[22] The advent of 3D printing technologies has permitted the fabrication of patient-specific scaffolds/implants that have controlled overall geometries and internal architectures.[23] Several 3D printing strategies, such as fused deposition modelling (FDM) and selective laser sintering (SLS) have been used to create architecture/geometry-defined implants and scaffolds using polymers, metals, glasses and ceramics.[22,24–29] However, the evaluation of surface topography of 3D printed scaffolds on cell behaviour has been under-explored. The strut surfaces of 3D printed scaffolds in most reports are smooth and fail to resemble the micro-/nano-topographies of the ECM. There has been only few research including one of ours on stem cell-topography interactions in 3D printed scaffolds.[30–32] Whilst understanding the topography-mediated stem cell differentiation in 3D is crucial for designing tissue engineering scaffolds, the range of topographies introduced to 3D printed scaffolds has been quite narrow, for instance, the strut surface was randomly roughened either by post printing etching or phase inversion during printing[30,31], limiting the capability of utilising the topography of 3D printed scaffolds to direct stem cell differentiation. In addition, these current 3D printing approaches required additional post-printing etching[30] or deposition of polymer solution into solvent reservoir to allow non-solvent-induced phase separation[31] in order to obtain roughened surfaces, which could increase the complexity of the overall process.

Herein, a rapid, single-step extrusion-based 3D printing approach to directly fabricate high-resolution polymeric scaffold consisting of micro-struts (ca. 60 µm) with nano-porous (0.2-1µm)/micro-porous (1-2.4 µm) surfaces has been developed. This approach is based on direct ink writing of an agitated viscous polycaprolactone (PCL)/dichloromethane (DCM)

solution. Air-bubbles generated in the solution were approved to be critical for the formation of strut surface pores, which is a mechanism that has not been reported before. We have also demonstrated the impact of the micro/nano-porous strut surface on cell adhesion, proliferation, chondrogenic and osteogenic differentiation of MSCs in comparison to the non-porous strut surface. The strut pores showed drastically different effects on MSC morphology and adhesion in chondrogenic and osteogenic media. Strut pores promoted MSC differentiation in medium without soluble differentiation factors. However, the level of effect on chondrogenic and osteogenic differentiation was different in medium with soluble differentiation factors.

EXPERIMENTAL SECTION

Ink Preparation and Direct-Write 3D Printing of Scaffolds

Lattice scaffolds were designed by BioCAD software and fabricated by direct deposition of a viscous polycaprolactone (PCL)/dichloromethane (DCM) solution through a tapered tip (31G, 152 µm internal diameter, Integrated Dispensing Solutions, USA) using a 3D Discovery printer (regenHU, Switzerland) with a pressure of 6 bar and a printing speed of 1.0-3.0 cm/s. In creating porous surface on the micro-struts of the scaffold, a 57% (w/v) homogeneous PCL/DCM solution was agitated on a vortex mixer at 1900 rpm or 3200 rpm for 1 hour prior to 3D printing, which resulted in the formation of small bubbles in the polymer solution. For the scaffolds with non-porous strut surfaces, the non-agitated PCL/DCM solution was centrifuged at 13000 rpm for 10 min prior to 3D printing in order to get rid of bubbles. An air-flow was introduced during 3D printing to facilitate DCM evaporation resulting in rapid solidification of the structures. After printing, the scaffolds were immersed in ethanol/water mixture (7/3) for 1 hour to remove any residual DCM and sterilise the structures. The scaffolds used in differentiation studies had a macropore size of ca. 250 µm.

TGA and GC-MS

Residual DCM solvent in the 3D printed scaffolds (n=2) was primarily evaluated by a Discovery TGA (Thermal Analysis Instruments, UK) in a nitrogen atmosphere with a heating rate of $10^{o}C$/min. Quantification of the residual DCM in the 3D printed scaffolds at different times after printing (0 min, 1 h, 24 h) was performed using gas chromatography-mass spectrometer (GC-MS) equipped with a headspace analyser (ITQ with Trace 1300, Thermo Fisher Scientific, UK) and the operation condition following previously published protocol.[33] Scaffold ($0.4 \times 1 \times 0.5$ cm^3, weight of 49.8 mg) /virgin PCL material (as a control, weight of 50 mg) were immersed in 10 ml LC-grade DMSO (Sigma-Aldrich) for 24 h prior to subjecting to a GC-MS. Different concentration of DCM in 10 ml DMSO were used as standard solutions.

Surface Characterisations

The topographies, diameters of printed struts and pore interconnectivity of the 3D printed scaffolds were visualised by a scanning electron microscope (JEOL JSM-6490LV, UK). Cell-seeded scaffolds, fixed in 2.5% glutaraldehyde, post-fixed in 1% osmium tetroxide, dehydrated in increasing concentration of ethanol and hexamethyldisilizane (HMDS, Sigma-Aldrich), were used for SEM imaging of cell morphology. Quantitative analysis of pore morphology on the printed struts (n = 150) was performed using high magnification SEM images (20000x, n = 3) and an ImageJ software (NIH, USA). Roughness (a measurement of height deviations of peaks and valleys on a surface from the mean line) and height profiles of the strut surfaces were measured using a PeakForce Tapping® AFM (FastScan, Bruker, UK) with a commercially available AFM tips (MPP-12120-10, Bruker) at a scan field of 8µm×8µm and a scan rate of 1 Hz. Specific surface area of a whole scaffold structure was measured by Kr gas absorption

experiment using an accelerated surface area and porosimetry system (ASAP® 2420, Micromeritics, UK) and calculated based on Brunauer–Emmett–Teller (BET) theory.

Fibronectin Absorption

The scaffolds, after soaking in ethanol/water mixture (7/3) and washing in PBS, were incubated in 30 µg/ml fibronectin (Sigma-Aldrich, UK) solution under standard cell culture condition (37°C, 5% CO_2) with orbital shaking of 30 rpm overnight. The concentration of fibronectin used in this study corresponds to the concentration of fibronectin in standard tissue culture medium that contains 10% FBS.[34] Amount of fibronectin in the protein solution was measured with a Quick Start™ Bradford Protein Assay (Bio-Rad, UK). The amount of absorbed fibronectin was calculated by subtracting the initial amount of fibronectin with a residual amount in the protein solution. All samples and standards were done in triplicate.

Culture and Seeding of MSCs

Bone-derived human mesenchymal stem cells (MSCs) were immortalised, clonally selected (due to the variation in differentiation potential among clones), and maintained according to previous protocols.[35] The MSCs have been regularly assessed to ensure the capability of expansion without loss of tri-lineage differentiation potential. The scaffolds ($1 \times 1 \times 0.5$ cm^3), after sterilisation in 70% ethanol for 1 hour, were washed three times in PBS and incubated in expansion medium (Dulbecco's modified Eagle's medium (DMEM, high glucose) supplemented with 10% FBS, 1% non-essential amino acids, 1% L-glutamine and 1% antibiotic/antimycotic solution) overnight in 12-well plate. 5×10^5 cells were manually seeded onto each scaffold. Either chondrogenic medium (DMEM (low glucose), 50 µg/ml L-ascorbic acid phosphate, 40 µg/ml L-proline, 1% ITS+ and 1 mM pyruvate) with or without 10 ng/ml TGFβ$_1$ or osteogenic medium (αMEM, 10% FBS, 1% L-glutamine and 1% antibiotic/antimycotic solution, and 10

mM β-glycerophosphate) with or without 100 nM dexamethasone was subsequently added and the medium was changed every 2 days.

Evaluation of MSC Morphology

Morphologies of MSCs, 24 hours following the initial attachment to the scaffold surfaces were assessed. 24 h was chosen as cell remained mostly as non-aggregated cells. Cross-sections of cell-seeded scaffolds were stained for investigating the organisation of actin filament using Alexa Fluor® 488 Phalloidin (Cell Signaling Technology, USA). The stained specimens were counterstained with Hoechst 33258 (Sigma-Aldrich) for nucleus staining and visualised by a Leica TCS LSI laser confocal microscope. An average cell area was analysed by ImageJ (n = 100). The average number of the surface micro-/nano-pores covered by an individual cell was calculated by dividing cell area with the average pore area of 10 SEM images of porous struts.

Chondrogenic Differentiation

MSC-seeded scaffolds were harvested at different cultivation times (day 1, 7, 14, and 28), washed with PBS and individually digested 500 µl papain digestive solution (280 µg/ml papain, 50 mM EDTA, 5 mM L-cysteine in Dulbecco's PBS pH 6.5, all from Sigma-Aldrich) at 45°C for 2 days. The supernatants of the digested samples were used for monitoring total DNA content using a Quant-iT^{TM} Picogreen® kit (Invitrogen). Dimethymethylene blue (DMMB, Sigma-Aldrich) and a hydroxyproline assay kit (QuickZyme Bioscience, UK) were used to measure the amount of secreted sulfated glycosaminoglycan (sGAG) and total collagen, respectively. All samples and standards were done in triplicate. Immunostaining of type II collagen was performed using primary antibody (MAB1330, Merck Millipore, UK) and secondary antibody labelled with Alexa Fluor 488 (Abcam, ab150113). The sections were counterstained with Hoechst 33258 and imaged using a Leica TCS LSI laser confocal microscope.

Osteogenic Differentiation

MSC-seeded scaffolds, after cultivation for 1, 7, 14 and 28 days in osteogenic medium, were harvested, washed with ice-cold PBS, homogenised in RIPA lysis buffer containing Halt^{TM} protease inhibitor cocktails (Thermo Fisher Scientific, UK) and then freeze-thawed for 3 cycles to promote cell lysis. Alkaline phosphatase (ALP) activity was detected using the clear supernatants from cell lysates and an ALP fluorometric assay kit (Source Bioscience, UK). Osteocalcin production was analysed using a human osteocalcin sandwich ELISA kit (Invitrogen) and following the manufacturer's protocol. All samples and standards were done in triplicate. Cell-free scaffold samples were used as negative controls.

Statistical Analysis

All values in this study were reported as mean or mean ± standard deviation (SD). Statistically significant differences were analysed using Student's T-test or One-way ANOVA with Tukey's post hoc test. *, **, ***, or **** indicated statistically differences with $p<0.05$, $0.005<p<0.05$, $0.001<p<0.05$, and $p<0.001$, respectively.

RESULTS AND DISCUSSION

Formation of Micro-/Nano-Pores on Micro-Struts of 3D Printed Scaffolds

Polymeric scaffolds consisting of micro-struts (diameter ca. 60 µm) with 100% interconnected pores were printed by direct deposition of a viscous PCL/DCM solution through a micro nozzle (152 µm diameter) (**Figure 1A**). The 57% (w/v) PCL/DCM solution was selected as it was able to flow, which eased transferring of the solution into printing cartridges, and minimised strut spreading by rapid evaporation of the solvent. The diameter of the struts of the structures obtained in this study (ca. 60 µm) was significantly smaller than the nozzle and comparatively

smaller than struts in polymeric scaffolds fabricated previously by FDM.[24–28] This ''thinning'' effect was attributed to the interplay between the printing speed and the dispensing rate of the polymer solution. It has been shown that a nozzle can print struts with resolution much finer than the nozzle diameter by stretching the extruded polymer solution.[36]

Agitation of the 57% (w/v) PCL/DCM for 1 hour prior to 3D printing generated bubbles in the solution and resulted in micro-/nano-pores (the diameter range of 0.2 to 2.4 µm) on the strut surfaces after DCM evaporation whilst there were no pores when the non-agitated solution was used (**Figure 1B**). The pores existed only on the surface of the struts (**Figure 1A and Figure S1**). In contrast, conventional porogen-leaching methods can generate pores inside the struts (**Figure S1**), which compromises mechanical properties. Different degree of agitation led to different amount of bubbles in the polymer solution that caused different surface pore density and pore size (**Figure 1C**). Pore density on the struts increased with the agitation intensity. By visual observation, the bubbles disappeared once the pressure was applied to the printing cartridge. No pores were observed on the printed struts when the agitated PCL/DCM solution remained undisturbed for 12 hours in which all visible small air bubbles in the solution floated up and disappeared (**Figure S2A**). In addition, boiling of the PCL/DCM solution at 80ºC without agitation also created bubbles in the solution and resulted in pores on the printed struts (**Figure S2B**). This suggests the presence of pores on strut surfaces was attributed to the formation of bubbles in the polymer solution.

The viscosity/concentration of the polymer solution and DCM evaporation rate also affected the formation of micro-/nano-pores on the surfaces of the printed struts. Bubbles in diluted agitated PCL/DCM i.e., 45% (w/v), migrated towards the top air-liquid interface of the solution and became disappeared more quickly (1h after), which eventually contributed to less pores on the

resultant printed struts (**Figure S2C**). This suggested the viscosity of the solution needs to be high enough to stabilise bubbles. Less or no pores was also observed at the area close to the strut intersections (**Figure S3**). This suggested that the formation of pores also depended on the evaporation rate of the solvent because the accumulation of polymer solution at these intersectional regions led to longer DCM evaporation time.

It has been shown that phase separation of a polymer solution during solvent evaporation plays a key role in generating different surface morphologies on the surface of polymer fibres created by polymer/volatile solvent systems.[37–39] Rapid solvent evaporation contributes to immediate traversing of the system across the phase diagrams to the unstable region, permitting the settlement of the polymer-rich and polymer-lean phases and resulting in the formation of fine porous morphology.[37,38] The condensation of water on fibre surface due to the rapid cooling caused by solvent evaporation was also used to explain the formation of surface pores.[39] However, in our study the formation of bubbles in the polymer solution seemed to be a prerequisite for the formation of pores, which has not been reported before. It is worth noting that previous studies on surface pores were observed on electrospun fibres which have a smaller diameter compared to the struts in this study.

We postulate that the reason why pores are only on strut surface but not in the core may be due to the migration of air bubbles towards the solvent-air interface (the outermost surface of struts), which render an imprint in the form of pore on the strut surface. In this process, evaporation rate of DCM would be an important factor in controlling the surface pore density. Slow evaporation rate (e.g., at the strut intersectional regions) allowed time for the bubbles at the polymer-air interface to coalesce by surface tension leaving rough/non-porous surface whilst fast evaporation rate led to immediate formation of a surface pore from an individual bubble. The slower

evaporation rate of DCM in the core of the struts may also allow time for the bubbles to coalesce, which resulted in no pores in the strut core.
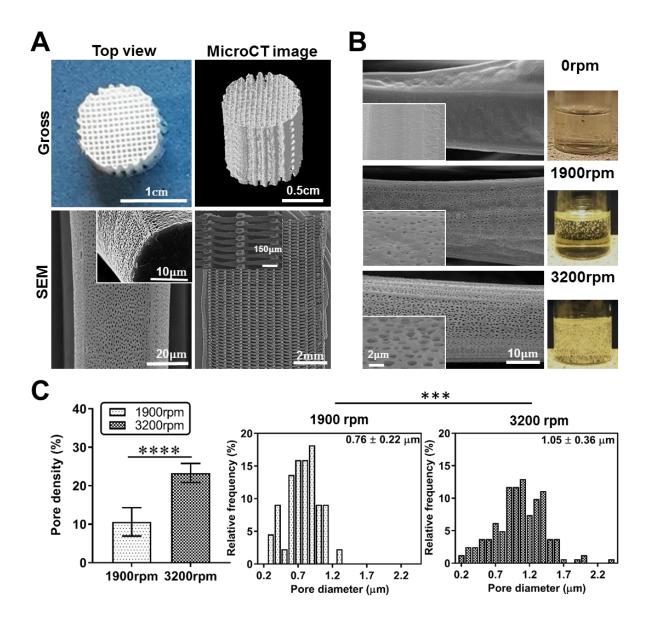

Figure 1. (A) 3D printed 1cm-tall PCL scaffold with strut diameter of approximately 60 µm and 100% interconnectivity. Inset showed pores only exist at the strut surface (B) Bubbles in the PCL/DCM solution generated by agitation and the porous topographies on the struts. Insets are high resolution SEM micrographs showing strut surface pores. (C) Strut surface pore density

(pore area/total area) and size distribution. All data represents mean ± SD (SEM images of 3 (n=150)). ***, **** indicate 0.001<*p*<0.05 and *p*<0.001, respectively.

Figure 2 showed further controlling of surface pore morphology and alignment (in relation to the printing direction) by changing the printing speed. Under the same extrusion pressure, increasing printing speed from 1.0 and 2.0 cm/s to 3.0 cm/s attenuated the printed strands (Figure 2B) and caused more elongated elliptical pores (Figure 2C). 63.7 ± 7.3% of the surface pores using the printing speed of 3.0 cm/s were highly aligned (angles < 10° [8]) compared to 19.5 ± 5.5% and 34.3 ± 11.2% for printing speed of 1.0 and 2.0 cm/s, respectively (Figure 2D). The pore diameter using the printing speed of 3.0 cm/s was 1.3 ± 0.4 µm compared to 1.0 ± 0.3 µm and 1.0 ± 0.4 µm for the speed of 1.0 cm/s and 2.0 cm/s, respectively. In addition, pore density was also reduced when the printing speed of 3.0 cm/s was used (Figure 2F).
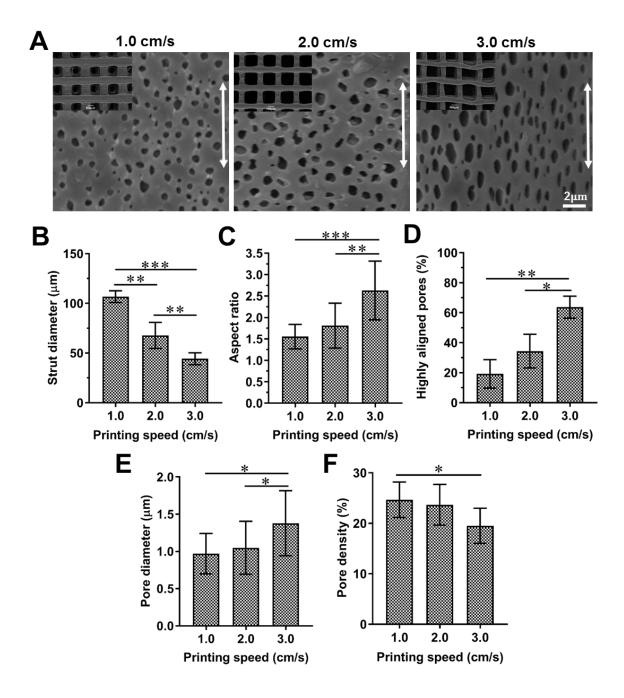
Figure 2. (A) SEM images showing the effect of printing speed on strut surface pore morphology. Arrows represent printing direction and insets show top views of the printed scaffolds. (B) Effect of printing speed on the strut diameter (n=10), (C) surface pore circularity, (D) pore alignment, (E) pore sizes and (F) pore density. Pore angle less than 10° was defined as

"highly aligned". All data represents mean ± SD with statistical difference (*$p<0.05$, **$0.005<p<0.05$, ***$0.001<p<0.05$). n=150 (from three SEM images)

Roughness and Surface Area of Micro-/Nano-Porous Strut Surfaces

Porous strut surfaces were evaluated by AFM. The representative height traces (mean height value was levelled to zero) from the struts surfaces showed the range of pore depth of approximately 76-175 nm (**Figure 3A**). Within 8×8 μm^2 of the analysis area, the micro-/nano-porous surfaces possessed approximately 1.5 times higher surface area than that of the non-porous surfaces (**Figure 3B**). Roughness (R_q) of the porous struts was 95 nm and approximately 2 times higher than that of non-porous surfaces (51 nm, **Figure 3C**). Previous studies using 2D titanium substrates and 3D printed scaffolds with roughened struts reported that the surface roughness of ca. 110-1300 nm can promote osteogenic differentiation of MSCs[30,31,40] whilst rougher 2D substrate surface (R_q above 2 μm) appeared to promote chondrogenic differentiation.[31] In addition to AFM analysis, measurement based on an accelerated physisorption of krypton gas showed the total amount of available surface area of a scaffold consisting of porous struts was 0.139 m^2/g, 4 times higher than the scaffolds with non-porous struts (**Figure 3D**). Due to increased surface area, more fibronectin absorption was also observed for the scaffolds with porous struts compared to those with non-porous surfaces (**Figure 3E**). The significant increase in surface area of the porous PCL struts will lead to more contact area with water. However, these pores are shallow and restricted to the surface. In addition, the amount of water that will be absorbed by PCL with surface pores is likely to be similar to PCL with a smooth surface as the pores are only present on the surface. Therefore, the degradaton rate may not be signiciantly affected by the presence of surface pores..
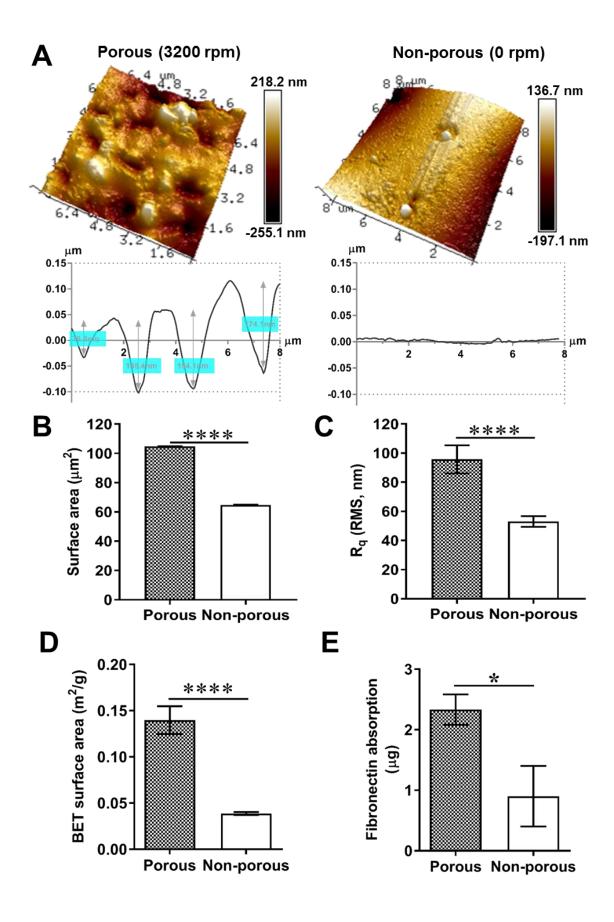
A Porous (3200 rpm) Non-porous (0 rpm)

218.2 nm 136.7 nm

−255.1 nm −197.1 nm

B

C

D

E

16

Figure 3. (A) Surface topographies with representative height traces of the 3D printed struts measured using AFM. Mean values of the surfaces were levelled to zero. (B) Surface area and (C) root mean squared roughness (R_q) of the strut surfaces measured using AFM. (D) Specific surface area of scaffolds with porous and non-porous struts measured using physisorption of krypton gas. (E) Fibronectin absorption onto the scaffolds with -porous or non-porous struts. All quantitative data represents mean ± SD (n = 3). *, **** indicate $p<0.05$ and $p<0.001$, respectively.

Solvent Residuals in the 3D Printed Scaffolds

As the direct writing fabrication process employed DCM as a solvent, residual DCM in the scaffolds after solvent evaporation may compromise biocompatibility and be a concern for clinical translation of these scaffolds. A thermogravimetric analysis (TGA) was carried out to quantify the remaining DCM in the scaffolds (un-washed, 24 h after printing) compared to the scaffolds that were immediately washed in 70% ethanol after printing (**Figure 4A**). Virgin PCL material without being dissolved in DCM was also included in the study as a control. In comparison to the virgin PCL material, TGA profiles of the un-washed and washed scaffolds showed no weight changes within the DCM evaporation temperature region (40°C to 100°C), suggesting the residual DCM solvent in the 3D printed scaffolds after printing was undetectable based on the TGA sensitivity of 0.1 µg for a typical 10 mg sample.

To achieve a better sensitivity, quantification of DCM residues in the 3D printed scaffold at different times after 3D printing (0 min, 1h, and 24 h) was also carried out using GC-MS (detection limit of 0.1 ppm, **Figure 4B**). The chromatograms (**Figure S4**) showed a significant decrease in the area under DCM peak (m/z of 84) when the scaffolds were left exposed to air for

1 hour and 24 hours compared to those immediately after printing. The amount of residual DCM in the as-printed 3D printed scaffold were 436.2 ppm. After being exposed to air for 1 hour at room temperature to allow DCM evaporation, the DCM residue was considerably decreased to 19.0 ppm and to 13.8 ppm after 24 hours. A trace amount of DCM residual in the virgin PCL material was also detectable (11.2 ppm). The DCM residue in the scaffold at all time points was significantly lower than the concentration limit (600 ppm) of DCM in pharmaceuticals regulated by European Medicines Agency in the ICH guideline Q3C for residual solvent.[41] This suggested that the small size of the struts (ca. 60 µm) may contribute to the maximum evaporation of DCM, which would be beneficial for the scaffolds to be used as a tissue implant without compromising biocompatibility.
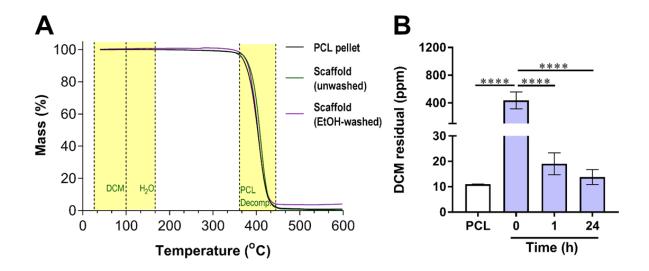

Figure 4. (A) Thermogravimetric analysis (TGA) profiles of the 3D printed PCL scaffolds (washed or un-washed in 70% ethanol after printing) and virgin PCL material. 40-100°C is expected as a region where DCM evaporation occurs. (B) Quantification of residual DCM in 3D printed scaffolds (at 0, 1 and 24h) compared to virgin PCL measured by GC-MS. The data represents mean ± SD (n=3) with statistically significant difference (****$p<0.001$).

Seeding Efficiency of MSCs

As the scaffolds consist of fine struts, the strut curvature was relatively bigger than scaffolds created in other studies.[24–28] Cell seeding efficiency can be compromised by increased curvature as cells can readily roll off the struts. To test the retention of cells after seeding, scaffolds with different macropore sizes (edge-edge spacing between struts) were fabricated to assess cell seeding efficiency. Immortalised MSCs were used in our studies as their tri-lineage differentiation potential have been demonstrated.[35] However, it was important to carry out clonal selection and regular investigation on their tri-lineage differentiation capability. It is worth noting that these immortalised MSCs cannot reflect the variation often seen in non-immortalised MSCs from different donors. MSC-seeding efficiency was assessed by comparing DNA content of the MSCs attached in the $1 \times 1 \times 0.5$ cm^3 scaffolds (3 h after initial seeding) to the DNA content of the starting total number of cells (5×10^5 cells). The results indicated a decreasing cell seeding efficiency with increasing macropore size (**Figure 5**). However, cells on the scaffolds with 50-µm macropores populated relatively quickly within 7 days. A cell layer covered the top of the scaffold, which would stop mass transport into the central region. Despite exhibiting lower cell seeding efficiency compared to 150µm-macropores, the scaffolds with 250-µm macropores were chosen for the subsequent studies as the size was within the range of reported optimal macropore size (200-700 µm) for chondrogenic and osteogenic differentiation.[25,42–44]
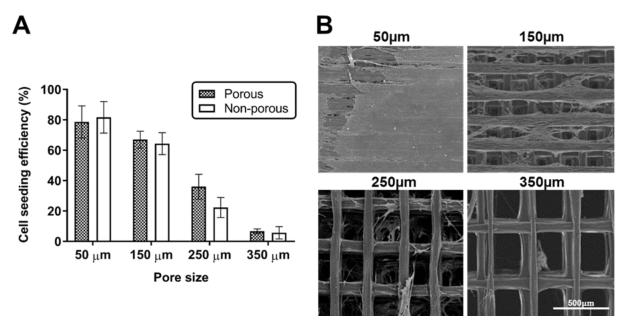
Figure 5. (A) Cell seeding efficiency (%) of MSCs in the 3D printed scaffolds with porous or non-porous struts and different pore sizes after 3h of initial seeding. All data represents mean ± SD (n = 3). (B). SEM images (top-view) of MSC adhesion to the 3D printed scaffolds with non-porous struts and different pore sizes at day 7. MSCs (5×10^5 cells) were seeded onto a $1 \times 1 \times 0.5$ cm^3 scaffolds with different pore sizes and cultured in expansion medium.

MSC Adhesion, Proliferation and Differentiation

Topography-mediated cell differentiation is a complex process and has been explored in many studies using 2D substrates with topographical features/roughness generated by various surface modification methods such as chemical etching, lithography and moulding.[3,9,14,45] Porous substrates have been found to promote osteogenic differentiation.[10,16,46] whilst how porous topography affects chondrogenic differentiation has been unknown. The effect of porous topography in 3D printed scaffolds on MSC differentiation into chondrogenic or osteogenic lineage has not been reported before.

Figure 6 showed the representative morphologies of MSCs after culturing for 24 hours in chondrogenic differentiation medium supplemented with TGFβ$_1$. MSCs on the micro-/nano-porous struts exhibited significantly larger spreading area than those on the non-porous struts (667±107 *vs* 142±22 μm^2) with the formation of long filopodia. On average a cell including cell body and filopodial processes covered approximately 192 micro-/nano-pores. In addition, protrusion of cell membrane as cell blebs was found (**Figure 6**, **left panel**), which can generally be observed during cell spreading and migration.[47] In contrast, MSCs on non-porous struts were rounded with the formation of relatively shorter cellular processes (**Figure 6, right panel**). Actin cytoskeleton seemed to form thick bundles at cell periphery on both porous and non-porous struts. The porous topography appeared to induce MSC spreading and the formation of long filopodia at day 1. However, MSCs on the non-porous struts started to spread at day 3 and eventually showed elongated morphology at day 28 (**Figure S5**).
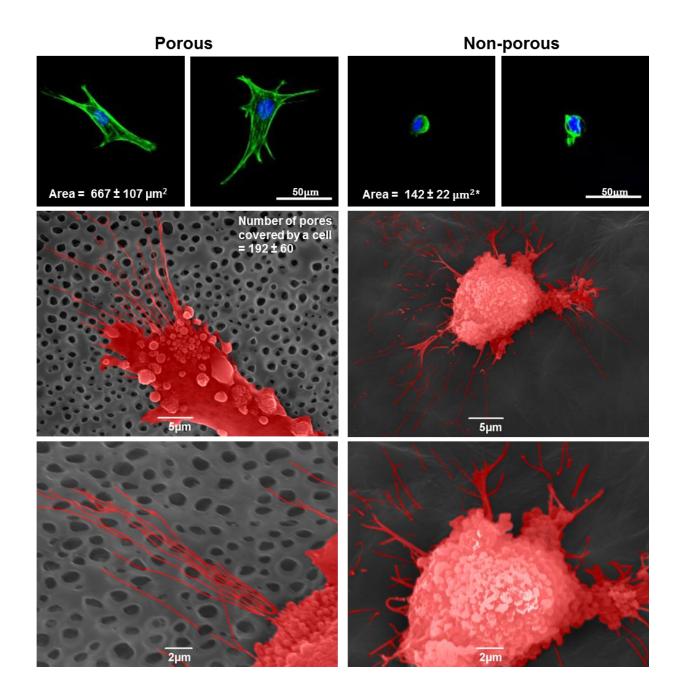
Figure 6. The representative confocal microscope images showing initial MSC morphology, organisation of actin cytoskeleton (green) and cell nucleus (blue) and the representative falsely-coloured SEM images of MSCs on the struts with or without pores at day 1. MSCs were cultured in chondrogenic medium containing 10 ng/ml TGFβ$_1$. Cell area (n = 100) and the number of the

surface micro-/nano-pores covered by an individual cell was analysed by ImageJ and * indicated statistically significant difference of cell area between porous and non-porous surfaces ($p<0.05$).

In osteogenic differentiation medium supplemented with dexamethasone (**Figure 7**), MSCs on the porous struts displayed less spreading morphology compared to MSCs on non-porous struts (cell area of 571 ± 71 vs 1105 ± 123 μm^2), which is opposite to that observed in chondrogenic medium. An MSC with filopodia on the porous struts covered approximately 164 micro-/nano-pores and thick actin bundle arranged at the cell periphery was found. MSCs on the non-porous struts displayed a larger spread, flatten morphology with parallel actin filaments extending across entire cytoplasm and the presence of filopodia protrusion beyond the noticeable lamellipodium edge.
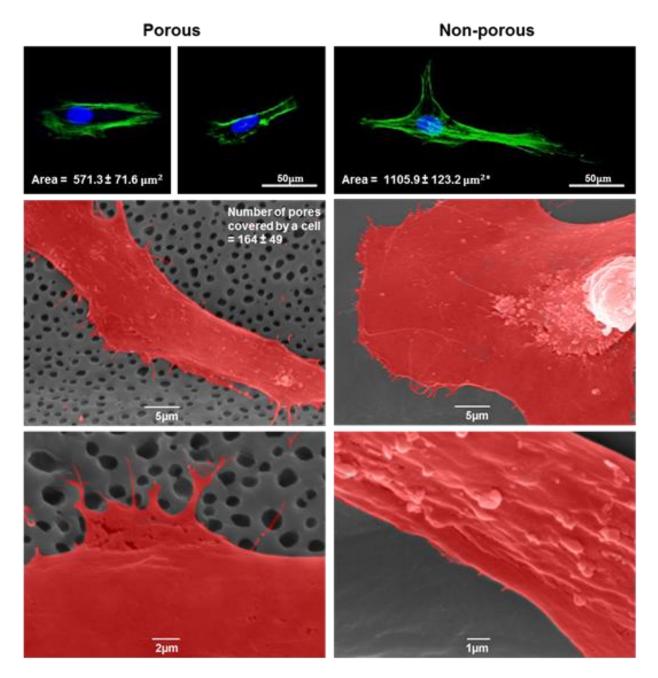
Figure 7. The representative confocal microscope images showing initial MSC morphology, organisation of actin cytoskeleton (green) and cell nucleus (blue) and the representative falsely-coloured SEM images of MSCs on the struts with or without pores at day 1. MSCs were cultured in osteogenic medium containing 100 nM dexamethasone. Cell area (n = 100) and the number of the surface micro-/nano-pores covered by an individual cell was analysed by ImageJ and *

indicated statistically significant difference of cell area between porous and non-porous surfaces ($p<0.05$).

It was assumed that MSCs actively probe the external environment on the porous topography upon adhesion to gather environmental information from the material surface. More elongated filipodia were observed on the porous struts in both differentiation conditions, which suggests that the pores made the MSCs more exploratory about their environment as filopodia are the machinery that cells employ to sense their surroundings.[48] Many filopodia crossed several pores as evidenced from the SEM images, which shows that the size of pores did not physically stop but appeared to promote the spreading of filopodia.

Filopodial protrusions have been thought to initiate integrin receptor clustering and focal adhesion protein recruitment before potential stem cell differentiation.[48] It is possible that the pores on the strut surface promoted the clustering of integrins as the pores do not offer any ligands for integrin binding. The spacing of integrin ligands have been studied at the nano-scale using nanoimprint lithography. Clustering of at least 4 liganded integrins within approximately 60 nm has been identifed to dramatically increase cell spreading and adhesion.[49] However, the effect of clustering of liganded integrins caused by topography at micro-scale on cell adhesion and spreading has not been reported. Our results suggest that micro-scale integrin clustering may also affect MSC adhesion and spreading. 2D substratates with chemical patterns of cell-binding fibronection dots with varied micro-scale spacings have shown that spacing between ligands and the size of ligand dots have a profound effect on cell adhesion and spreading. A distance of 5-25 µm between fibronectin dots was critical for cell spreading whilst cell could not spread when the dot spacing was above 30 µm.[50] The molecular mechanism for the dramatic difference in cell

spreading following initial cell attachment is beyond the scope of this study. However, it would be interesting to explore this further in the future using molecular biology tools.

Within the first week of cultivation (D1-D7), MSCs with larger spreading areas and well-developed cell protrusions (MSCs on the porous struts in chondrogenic medium and MSCs on non-porous struts in osteogenic medium) proliferated faster than those with smaller spreading areas/filopodial protrusions whilst the latter also reached the stationary phase later (**Figure 8**). It appeared that the cells that spreaded faster showed earlier cell division (D1-D7). It is worth noting that porous surface topography, whilst promoting spreading and proliferation of MSCs in the chondrogenic differentiation medium, limited spreading and proliferation of MSCs in osteogenic differentiation medum, indicating the interplay between surface topography and biochemical differentiation factors. The increase in cell spreading area has been found to be associated with increased actin-integrin binding and clustering[51], which are important for transducing strong proliferative signals, driving G1/S phase cell cycle progression, through focal adhesion kinase (FAK).[52]
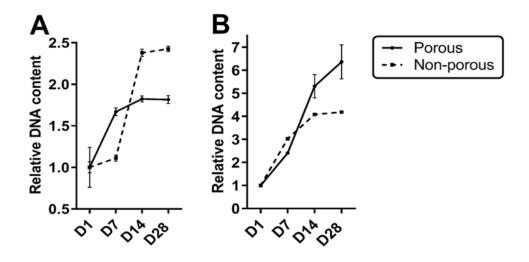
Figure 8. MSC proliferation on the porous and non-porous struts over 28 days (n = 3) in chondrogenic (A) and osteogenic differentiation conditions (B) measured by DNA content normalised to day 1. All data represents mean ± SD.

Organisation of actin cytoskeleton following initial cell-material interaction has been shown to influence cell morphologies and subsequent stem cell differentiation, particularly osteogenic and adipogenic differentiation.[53] Based on the previous studies using 2D substrates with topographies, chondrogenic differentiation-topography interaction has been significantly less studied compared to osteogenic and adipogenic differentiation in which cell adhesion elicits cytoskeleton reorganisation and molecular signalling pathways. In order to investigate how micro-/nano-porous topography in a 3D printed scaffold affect chondrogenic and osteogenic differentiation of MSCs, 4-week *in vitro* differentiation studies were carried out.

In chondrogenic differentiation medium with $TGF\beta_1$, despite displaying well-spread morphology with longer filopodial protrusion and faster proliferation rate (**Figure 6 and 8**), the chondrogenic differentiation of MSCs on the porous struts, as indicated by sGAG secretion **(Figure 9A)** and collagen II production (**Figure 9B**), was similar to those with less-spread, rounded morphology on the non-porous struts. It has been shown that rounded cell morphology is beneficial for chondrogenesis.[54,55] A study by Gao et al demonstrated that MSCs on micropatterned substrates where cell spreading and flattening were limited upregulated chondrogenic gene markers i.e., SOX9 and Col2A1.[18] In addition, it has been postulated that the absence of cell-matrix adhesion in the pellet culture acts as a permissive cue for chondrogenesis.[18] Quantification of collagen II production from fluorescence images of MSC-seeded scaffolds at day 28 also showed no significant difference between the porous and non-porous surface scaffolds (**Figure 9C**). In

contrast, in the medium without TGFβ1, chondrogenic differentiation was enhanced by the porous topography as evidenced by the increased levels of chondrogenic markers (sGAG and collagen II production). MSC morphology at day 1 on the non-porous surface in the absence of TGFβ1 showed a spindle-like shape which is markedly different from those in the presence of TGFβ1 (round shape) (**Figure S6**). This suggested that TGFβ1 can override the topographical effect on cell spreading and chondrogenic differentiation.
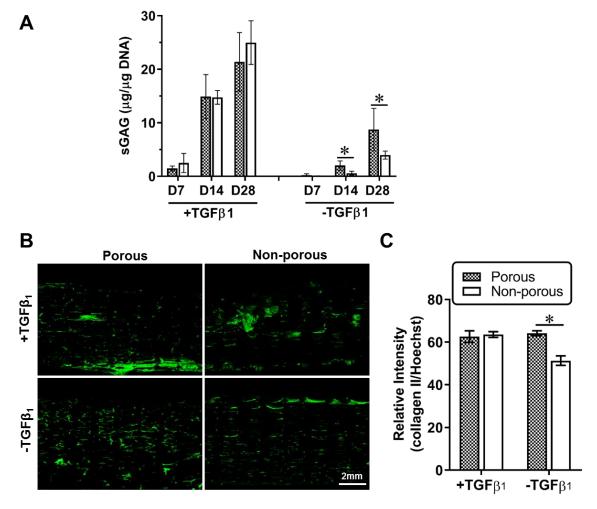

Figure 9. (A) Chondrogenic differentiation of MSCs cultured in 3D printed scaffolds with porous or non-porous struts over 7, 14 and 28 days characterised by the contents of sGAG normalised to DNA (n=3). (B) Fluorescent images (longitudinal cross-sections of scaffolds showing top to bottom) showed the presence of collagen type II (green) in scaffolds with porous

or non-porous struts in chondrogenic medium with TGFβ$_1$ for 28 days. (C) Quantified collagen II content from the fluorescent images. All graphical data represents mean ± SD (n = 3),* $p<0.05$.

As morphology and alignment of the surface micro-/nano-pores could be tailored by our 3D printing approach, we investigated the effect of pore alignment on MSC spreading, proliferation and chondrogenic differentiation. The scaffolds with aligned surface pores (63.7% alignment) were created by printing scaffolds at the speed of 3.0 cm/s. Regardless of TGFβ$_1$ presence in the chondrogenic medium, MSCs on the aligned porous topography exhibited less spreading (**Figure 10A**), slower proliferation (**Figure 10B**) but greater chondrogenic differentiation as indicated by sGAG production (**Figure 10C**), when compared to those on the non-aligned porous (34.3 % alignment). When the pores were more aligned, the area of smooth surface between pores appeared to increase, which was confirmed in **Figure 2F** that showed reduced pore density at the speed of 3.0 cm/s. Combined with the observation that MSCs displayed round morphology on non-porous surfaces **(Figure 6)**, it is postulated that the ratio between pores and smooth surface significantly affects MSC spreading in chondrogenic differentiation medium.

There was a mixture of nano- (< 1 µm) and micropores (> 1 µm) on the strut surface in our study. The competitiveness and synergism between the micro- and nano-topographies on cell adhesion and migration was investigated in a previous study.[8] However, the surface micro-pores and nano-pores fabricated in our study were randomly distributed throughout the strut surfaces, which makes it challenging to investigate if there was a synergistic or competitive effect between micro- and nano-pores on cell adhesion and differentiation.

A

Non-aligned pores   **Aligned porores**

+TFGβ₁

No of pores covered by a cell = 164 ± 49

10μm Cell area = 667 ± 107 μm²

No of pores covered by a cell = 24 ± 8

10μm Cell area = 134 ± 33 μm²*

-TFGβ₁

No of pores covered by a cell = 215 ± 61

10μm Cell area = 741 ± 87 μm²

No of pores covered by a cell = 77 ± 21

10μm Cell area = 612 ± 98 μm²

B

Relative DNA content

+TFGβ₁   -TFGβ₁

— Porous
--- Aligned Porous

D1 D7 D14 D28   D1 D7 D14 D28

C

sGAG (μg/μg DNA)

Porous
Aligned Porous

*

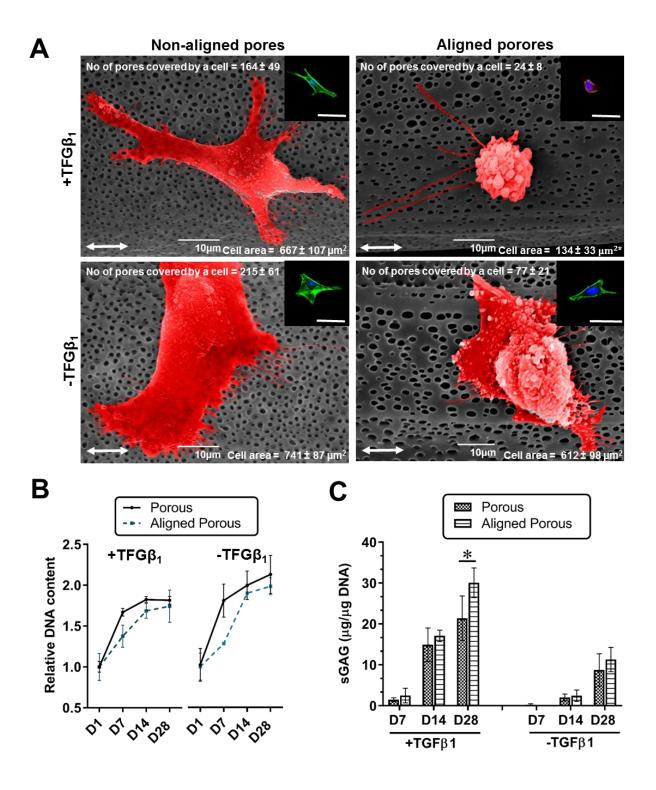D7 D14 D28   D7 D14 D28
+TGFβ1   -TGFβ1

Figure 10. (A) Representative falsely-coloured SEM images of MSCs on struts with non-aligned pores and aligned pores. The insets are representative confocal microscope images showing MSC morphology, actin cytoskeleton (green) and cell nucleus (blue) at day 1. Cell area (n = 100) and the number of surface pores covered by an individual cell were analysed by ImageJ. White double-head arrows show the printing direction. (B) Proliferation measured by DNA content normalised to day 1 (n = 3) and (C) chondrogenic differentiation of MSCs on the struts with non-aligned and aligned pores over 28 days characterised by the contents of sGAG normalised to DNA (n = 3). MSCs were cultured in chondrogenic medium with or without 10 ng/ml TGFβ$_1$. All data represents mean ± SD (* $p<0.05$).

In osteogenic inductive medium with dexamethasone, MSCs on porous struts displayed increased osteogenic differentiation as indicated by increased enzymatic activity of alkaline phosphatase at day 14 (ALP, a marker of early stage osteogenesis, **Figure 11A**) and considerably higher production of osteocalcin at day 28 (a marker of late stage osteogenesis, **Figure 11B**) than those on non-porous struts. It was hypothesised that the organisation of actin cytoskeleton influenced cellular tension, which subsequently exerted an impact on osteogenic differentiation. As MSCs on the porous struts showed thick actin bundle arranged at the cell periphery and were more differentiated compared to those on the non-porous struts with parallel actin filaments and were less differentiated, this finding agreed with the previous study in which the osteogenic differentiated MSCs showed actin cytoskeleton as a few, thick filament at the outermost cell periphery (cortical organisation) whilst undifferentiated cells showed the parallel arrangement.[53] In the medium without dexamethasone, osteogenic differentiation was also enhanced by the porous topography as evidenced by the increased levels of osteocalcin (**Figure**

11B) although MSCs on non-porous surface appeared to enter differentiation stage earlier than those on the porous topography as demonstrated by increased ALP activity at D14 (**Figure 11A**, the right panel). This suggests that there is a synergistic effect between dexamethasone and porous topography for osteogenic differentiation.
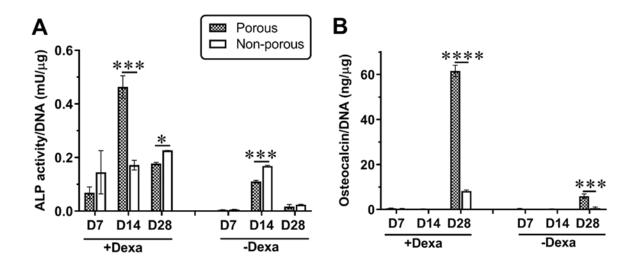

Figure 11. Osteogenic differentiation of MSCs cultured in 3D printed scaffolds with porous or non-porous strands over 7, 14 and 28 days characterised by ALP activity (A) and osteocalcin production (B) normalised to DNA. The MSC-seeded scaffolds were cultured for 28 days in osteogenic medium with or without 100 nM dexamethasone. All data represents mean ± SD (n = 3). $*$ $p<0.05$, $***$ $0.001<p<0.05$, $****$ $p<0.001$.

Overall, we successfully incorporated a new topographical feature on micro-struts of a 3D printed PCL scaffold in the form of micro-/nano-scale pores and permitted the studies of how micro-/nano-topography regulates cell morphology, actin organisation and differentiation of MSCs in 3D. These micro-/nano-pores on strut surfaces have rendered 3D printed PCL scaffolds bio-instructive in which both chondrogenic and osteogenic differentiation of MSCs were

promoted in the absence of soluble biochemical factors. It is possible that the micro-/nano-porous struts might modulate the distribution pattern of adhesion-promoting ligands, such as integrin-binding domains of fibronectin, found in cell culture medium with FBS[34], which was used to immerse the scaffolds for 24 h before cell seeding. Distribution patterns of cell adhesion ligands on the micro-/nano-porous surfaces may differ from the non-porous surfaces, i.e., even dispersion on non-porous surface *vs* clumped dispersion separated by pores on micro-/nano-porous strut surfaces, which would lead to the different spacing of the adhesion clusters that could differentially contribute to mechanotransduction.[3,11]

We have also addressed topography-mediated MSC chondrogenesis, which has been under-explored compared to osteogenesis. Our scaffolds enabled the first exploration of topography-mediated MSC chondrogenesis in 3D printed scaffolds with defined micro-/nano-topographical features. Unlike other differentiation lineages, such as osteogenic and adipogenic, only a few attempts reported successful nano-topography-mediated chondrogenesis although the explored materials were 2D.[19,20]. Regarding to the evidence from 2D materials, it is worth noting the presence of nanopatterned surfaces is not always beneficial for promoting chondrogenic differentiation of MSCs unless round cell morphology and/or thick actin cytoskeleton arrangement at cell periphery were detected. Some nanopatterned 2D surfaces such as nano-pillar and nano-hole triggered round morphology and facilitated cell aggregation and chondrogenic differentiation of MSCs whilst chondrogenesis of MSCs on elongation-promoting topographies such as nano-grooves appeared to be compromised.[19,20] In literature, chondrogenic differentiation appears to require rounded cell shape and preventing focal adhesion attachment as evidenced by lower level of collagen II and aggrecan expression when MSCs were cultured on the integrin-binding peptide arginine-glycine-aspartic acid (RGD) surfaces.[56] In our study, MSCs

spreading more on porous struts at day 1 appeared to show low content of cartilage matrices at day 28. In addition, whilst MSCs on the non-patterned 2D PCL substrates from the aforementioned studies[19,20] exhibited well-spreading morphology with the least expression of chondrogenic markers even in the presence of TGFβ_3, MSCs on our 3D printed PCL scaffolds with non-porous struts displayed round morphology. This implies that topography-induced chondrogenesis is different between 2D and 3D systems. One possible reason is the curvature of the struts in 3D printed scaffolds. The material surfaces used in 2D materials are not curved whilst MSCs in this study resided on the micro-struts (diameter of ca. 60 µm) of a 3D printed scaffold, which is highly curved in relation to the size of a cell. A previous study has highlighted that surface curvature profoundly affected stem cell behaviours in which the spreading area of MSCs decreased with the increase of surface curvature and the decreased spreading cell area demonstrated improved adipogenic differentiation.[57] Systematic investigation of how surface curvature influences cell morphology, chondrogenic and osteogenic differentiation of MSCs in 3D printed scaffolds remains to be further explored.

CONCLUSION

A rapid, single-step extrusion-based 3D printing approach to directly create high-resolution polymeric scaffolds consisting of micro-struts with micro-/nano-porous surfaces has been developed. Agitation to introduce air bubbles in the polymer solution was found to be a prerequisite for the formation of micro-/nano-porous struts, which was different from other reported mechanisms for the formation of surface pores. The density, size, and alignment of these pores can be controlled by changing the degree of agitation or the speed of printing. The scaffolds fabricated in this study permitted the first exploration of how micro-/nano-porous topography influences the adhesion, chondrogenic and osteogenic differentiation of MSCs in 3D

printed porous scaffolds. The porous strut topography selectively affected the formation of filopodial protrusion, the organisation of actin cytoskeleton, cell morphology, and cell proliferation depending on the composition of the differentiation medium. In general, the surface pores promoted both chondrogenic and osteogenic differentiation in medium without soluble factors. The topographical effect was masked by TGFβ$_1$ in chondrogenic differentiation but generated a synergistic effect with dexamethasone in osteogenic differentiation. Our fabrication approach can potentially be used for a wide range of polymer biomaterials to create desirable architectures and topographies for directing stem cell differentiation.

ASSOCIATED CONTENT

Supporting Information.

The Supporting Information is available free of charge on the ACS Publication website.

Supplementary figure S1-S6 (PDF)

AUTHOR INFORMATION

Corresponding Author

*Email: jing.yang@nottingham.ac.uk

ACKNOWLEDGMENT

REFERENCES

(1)   Stevens, M. M.; George, J. H. Exploring and Engineering the Cell Surface Interface. *Science*. American Association for the Advancement of Science November 18, 2005, pp 1135–1138. https://doi.org/10.1126/science.1106587.

(2)   Trounson, A.; McDonald, C. Stem Cell Therapies in Clinical Trials: Progress and Challenges. *Cell Stem Cell*. 2015, pp 11–22. https://doi.org/10.1016/j.stem.2015.06.007.

(3)   Dalby, M. J.; Gadegaard, N.; Oreffo, R. O. Harnessing Nanotopography and Integrin-Matrix Interactions to Influence Stem Cell Fate. *Nat Mater* **2014**, *13* (6), 558–569. https://doi.org/10.1038/nmat3980.

(4)   Benoit, D. S. W.; Schwartz, M. P.; Durney, A. R.; Anseth, K. S. Small Functional Groups for Controlled Differentiation of Hydrogel-Encapsulated Human Mesenchymal Stem Cells. *Nat Mater* **2008**, *7* (10), 816–823. https://doi.org/10.1038/nmat2269.

(5)   Watt, F. M.; Huck, W. T. S. Role of the Extracellular Matrix in Regulating Stem Cell Fate. *Nat Rev Mol Cell Biol* **2013**, *14* (8), 467–473. https://doi.org/10.1038/nrm3620.

(6)   Wise, J. K.; Yarin, A. L.; Megaridis, C. M.; Cho, M. Chondrogenic Differentiation of Human Mesenchymal Stem Cells on Oriented Nanofibrous Scaffolds: Engineering the Superficial Zone of Articular Cartilage. *Tissue Eng Part A* **2008**, *15* (4), 913–921. https://doi.org/10.1089/ten.tea.2008.0109.

(7)   Zhou, X.; Novotny, J. E.; Wang, L. Anatomic Variations of the Lacunar-Canalicular

System Influence Solute Transport in Bone. *Bone* **2009**, *45* (4), 704–710. https://doi.org/10.1016/j.bone.2009.06.026.

(8)   López-Bosque, M. J.; Tejeda-Montes, E.; Cazorla, M.; Linacero, J.; Atienza, Y.; Smith, K. H.; Lladó, A.; Colombelli, J.; Engel, E.; Mata, A. Fabrication of Hierarchical Micro-Nanotopographies for Cell Attachment Studies. *Nanotechnology* **2013**, *24* (25), 255305. https://doi.org/10.1088/0957-4484/24/25/255305.

(9)   Khang, D.; Choi, J.; Im, Y.-M.; Kim, Y.-J.; Jang, J.-H.; Kang, S. S.; Nam, T.-H.; Song, J.; Park, J.-W. Role of Subnano-, Nano- and Submicron-Surface Features on Osteoblast Differentiation of Bone Marrow Mesenchymal Stem Cells. *Biomaterials* **2012**, *33* (26), 5997–6007. https://doi.org/10.1016/J.BIOMATERIALS.2012.05.005.

(10)   Popat, K. C.; Chatvanichkul, K.-I.; Barnes, G. L.; Latempa, T. J.; Grimes, C. A.; Desai, T. A. Osteogenic Differentiation of Marrow Stromal Cells Cultured on Nanoporous Alumina Surfaces. *J Biomed Mater Res Part A* **2007**, *80A* (4), 955–964. https://doi.org/10.1002/jbm.a.31028.

(11)   Dalby, M. J.; García, A. J.; Salmeron-Sanchez, M. Receptor Control in Mesenchymal Stem Cell Engineering. *Nat Rev Mater* **2018**, *3* (3), 17091. https://doi.org/10.1038/natrevmats.2017.91.

(12)   McMurray, R. J.; Gadegaard, N.; Tsimbouri, P. M.; Burgess, K. V; McNamara, L. E.; Tare, R.; Murawski, K.; Kingham, E.; Oreffo, R. O.; Dalby, M. J. Nanoscale Surfaces for the Long-Term Maintenance of Mesenchymal Stem Cell Phenotype and Multipotency. *Nat Mater* **2011**, *10* (8), 637–644. https://doi.org/10.1038/nmat3058.

(13)   Wilkinson, A.; Hewitt, R. N.; McNamara, L. E.; McCloy, D.; Dominic Meek, R. M.;

Dalby, M. J. Biomimetic Microtopography to Enhance Osteogenesis in Vitro. *Acta Biomater* **2011**, *7* (7), 2919–2925. https://doi.org/10.1016/J.ACTBIO.2011.03.026.

(14) Dalby, M. J.; Gadegaard, N.; Tare, R.; Andar, A.; Riehle, M. O.; Herzyk, P.; Wilkinson, C. D.; Oreffo, R. O. The Control of Human Mesenchymal Cell Differentiation Using Nanoscale Symmetry and Disorder. *Nat Mater* **2007**, *6* (12), 997–1003. https://doi.org/10.1038/nmat2013.

(15) Treiser, M. D.; Yang, E. H.; Gordonov, S.; Cohen, D. M.; Androulakis, I. P.; Kohn, J.; Chen, C. S.; Moghe, P. V. Cytoskeleton-Based Forecasting of Stem Cell Lineage Fates. *Proc Natl Acad Sci U S A* **2010**, *107* (2), 610–615. https://doi.org/10.1073/pnas.0909597107.

(16) Niu, H.; Lin, D.; Tang, W.; Ma, Y.; Duan, B.; Yuan, Y.; Liu, C. Surface Topography Regulates Osteogenic Differentiation of MSCs via Crosstalk between FAK/MAPK and ILK/β-Catenin Pathways in a Hierarchically Porous Environment. *ACS Biomater Sci Eng* **2017**, *3* (12), 3161–3175. https://doi.org/10.1021/acsbiomaterials.7b00315.

(17) Wang, W.; Zhao, L.; Wu, K.; Ma, Q.; Mei, S.; Chu, P. K.; Wang, Q.; Zhang, Y. The Role of Integrin-Linked Kinase/β-Catenin Pathway in the Enhanced MG63 Differentiation by Micro/Nano-Textured Topography. *Biomaterials* **2013**, *34* (3), 631–640. https://doi.org/10.1016/j.biomaterials.2012.10.021.

(18) Gao, L.; McBeath, R.; Chen, C. S. Stem Cell Shape Regulates a Chondrogenic versus Myogenic Fate through Rac1 and N-Cadherin. *Stem Cells* **2010**, *28* (3), 564–572. https://doi.org/10.1002/stem.308.

(19) Wu, Y. N.; Law, J. B. K.; He, A. Y.; Low, H. Y.; Hui, J. H. P.; Lim, C. T.; Yang, Z.; Lee,

E. H. Substrate Topography Determines the Fate of Chondrogenesis from Human Mesenchymal Stem Cells Resulting in Specific Cartilage Phenotype Formation. *Nanomedicine Nanotechnology, Biol Med* **2014**, *10* (7), 1507–1516. https://doi.org/10.1016/j.nano.2014.04.002.

(20) Wu, Y.; Yang, Z.; Law, J. B. K.; He, A. Y.; Abbas, A. A.; Denslin, V.; Kamarul, T.; Hui, J. H. .; Lee, E. H. The Combined Effect of Substrate Stiffness and Surface Topography on Chondrogenic Differentiation of Mesenchymal Stem Cells. *Tissue Eng Part A* **2017**, *23* (1–2), 43–54. https://doi.org/10.1089/ten.tea.2016.0123.

(21) Lim, Y. Bin; Kang, S. S.; Park, T. K.; Lee, Y. S.; Chun, J. S.; Sonn, J. K. Disruption of Actin Cytoskeleton Induces Chondrogenesis of Mesenchymal Cells by Activating Protein Kinase C-α Signaling. *Biochem Biophys Res Commun* **2000**, *273* (2), 609–613. https://doi.org/10.1006/bbrc.2000.2987.

(22) Rumiński, S.; Ostrowska, B.; Jaroszewicz, J.; Skirecki, T.; Włodarski, K.; Święszkowski, W.; Lewandowska-Szumieł, M. Three-Dimensional Printed Polycaprolactone-Based Scaffolds Provide an Advantageous Environment for Osteogenic Differentiation of Human Adipose-Derived Stem Cells. *J Tissue Eng Regen Med* **2018**, *12* (1), e473–e485. https://doi.org/10.1002/term.2310.

(23) Murphy, S. V; Atala, A. 3D Bioprinting of Tissues and Organs. *Nat Biotechnol* **2014**, *32* (8), 773–785. https://doi.org/10.1038/nbt.2958.

(24) Serra, T.; Planell, J. A.; Navarro, M. High-Resolution PLA-Based Composite Scaffolds via 3-D Printing Technology. *Acta Biomater* **2013**, *9* (3), 5521–5530. https://doi.org/10.1016/J.ACTBIO.2012.10.041.

(25)   Zein, I.; Hutmacher, D. W.; Tan, K. C.; Teoh, S. H. Fused Deposition Modeling of Novel Scaffold Architectures for Tissue Engineering Applications. *Biomaterials* **2002**, *23* (4), 1169–1185. https://doi.org/10.1016/s0142-9612(01)00232-0.

(26)   Ruiz-Cantu, L.; Gleadall, A.; Faris, C.; Segal, J.; Shakesheff, K.; Yang, J. Characterisation of the Surface Structure of 3D Printed Scaffolds for Cell Infiltration and Surgical Suturing. *Biofabrication* **2016**, *8* (1). https://doi.org/10.1088/1758-5090/8/1/015016.

(27)   Shor, L.; Güçeri, S.; Wen, X.; Gandhi, M.; Sun, W. Fabrication of Three-Dimensional Polycaprolactone/Hydroxyapatite Tissue Scaffolds and Osteoblast-Scaffold Interactions in Vitro. *Biomaterials* **2007**, *28* (35), 5291–5297. https://doi.org/10.1016/J.BIOMATERIALS.2007.08.018.

(28)   Woodfield, T. B. F.; Malda, J.; de Wijn, J.; Peters, F.; Riesle, J.; van Blitterswijk, C. A. Design of Porous Scaffolds for Cartilage Tissue Engineering Using a Three-Dimensional Fiber-Deposition Technique. *Biomaterials* **2004**, *25* (18), 4149–4161. https://doi.org/10.1016/j.biomaterials.2003.10.056.

(29)   Du, Y.; Liu, H.; Yang, Q.; Wang, S.; Wang, J.; Ma, J.; Noh, I.; Mikos, A. G.; Zhang, S. Selective Laser Sintering Scaffold with Hierarchical Architecture and Gradient Composition for Osteochondral Repair in Rabbits. *Biomaterials* **2017**, *137*, 37–48. https://doi.org/10.1016/j.biomaterials.2017.05.021.

(30)   Kumar, G.; Waters, M. S.; Farooque, T. M.; Young, M. F.; Simon Jr., C. G. Freeform Fabricated Scaffolds with Roughened Struts That Enhance Both Stem Cell Proliferation and Differentiation by Controlling Cell Shape. *Biomaterials* **2012**, *33* (16), 4022–4030. https://doi.org/10.1016/j.biomaterials.2012.02.048.

(31) Neves, S. C.; Mota, C.; Longoni, A.; Barrias, C. C.; Granja, P. L.; Moroni, L. Additive Manufactured Polymeric 3D Scaffolds with Tailored Surface Topography Influence Mesenchymal Stromal Cells Activity. *Biofabrication* **2016**, *8* (2), 025012. https://doi.org/10.1088/1758-5090/8/2/025012.

(32) Prasopthum, A.; Shakesheff, K. M.; Yang, J. Direct Three-Dimensional Printing of Polymeric Scaffolds with Nanofibrous Topography. *Biofabrication* **2018**, *10* (2), 025002. https://doi.org/10.1088/1758-5090/aaa15b.

(33) Panovska, A. P.; Acevska, J.; Stefkov, G.; Brezovska, K.; Petkovska, R.; Dimitrovska, A. Optimization of HS-GC-FID-MS Method for Residual Solvent Profiling in Active Pharmaceutical Ingredients Using DoE. *J Chromatogr Sci* **2016**, *54* (2), 103–111. https://doi.org/10.1093/chromsci/bmv123.

(34) Hayman, E. G.; Ruoslahti, E. Distribution of Fetal Bovine Serum Fibronectin and Endogenous Rat Cell Fibronectin in Extracellular Matrix. *J Cell Biol* **1979**, *83* (1), 255–259. https://doi.org/10.1083/jcb.83.1.255.

(35) Okamoto, T.; Aoyama, T.; Nakayama, T.; Nakamata, T.; Hosaka, T.; Nishijo, K.; Nakamura, T.; Kiyono, T.; Toguchida, J. Clonal Heterogeneity in Differentiation Potential of Immortalized Human Mesenchymal Stem Cells. *Biochem Biophys Res Commun* **2002**, *295* (2), 354–361. https://doi.org/10.1016/s0006-291x(02)00661-7.

(36) Yuk, H.; Zhao, X. A New 3D Printing Strategy by Harnessing Deformation, Instability, and Fracture of Viscoelastic Inks. *Adv Mater* **2018**, *30* (6), 1704028. https://doi.org/10.1002/adma.201704028.

(37) Megelski, S.; Stephens, J. S.; Bruce Chase, D.; Rabolt, J. F. Micro- and Nanostructured

Surface Morphology on Electrospun Polymer Fibers. *Macromolecules* **2002**, *35* (22), 8456–8466. https://doi.org/10.1021/ma020444a.

(38) Dayal, P.; Kyu, T. Porous Fiber Formation in Polymer-Solvent System Undergoing Solvent Evaporation. *J Appl Phys* **2006**, *100* (4), 043512. https://doi.org/10.1063/1.2259812.

(39) Yazgan, G.; Dmitriev, R. I.; Tyagi, V.; Jenkins, J.; Rotaru, G.-M.; Rottmar, M.; Rossi, R. M.; Toncelli, C.; Papkovsky, D. B.; Maniura-Weber, K.; et al. Steering Surface Topographies of Electrospun Fibers: Understanding the Mechanisms. *Sci Rep* **2017**, *7* (1), 158. https://doi.org/10.1038/s41598-017-00181-0.

(40) Takeuchi, K.; Saruwatari, L.; Nakamura, H. K.; Yang, J.-M.; Ogawa, T. Enhanced Intrinsic Biomechanical Properties of Osteoblastic Mineralized Tissue on Roughened Titanium Surface. *J Biomed Mater Res* **2005**, *72*, 296–305. https://doi.org/10.1002/jbm.a.30227.

(41) Expert Working Group, I. C. H. Impurities: Guideline for Residual Solvents Q3C(R4). In *ICH Harmonised Tripartite Guideline*; 2009; pp 1–20.

(42) Di Luca, A.; Ostrowska, B.; Lorenzo-Moldero, I.; Lepedda, A.; Swieszkowski, W.; Van Blitterswijk, C.; Moroni, L.; Sany, J.; Jorgensen, C. Gradients in Pore Size Enhance the Osteogenic Differentiation of Human Mesenchymal Stromal Cells in Three-Dimensional Scaffolds. *Sci Rep* **2016**, *6* (1), 22898. https://doi.org/10.1038/srep22898.

(43) Zhang, Z. Z.; Jiang, D.; Ding, J. X.; Wang, S. J.; Zhang, L.; Zhang, J. Y.; Qi, Y. S.; Chen, X. S.; Yu, J. K. Role of Scaffold Mean Pore Size in Meniscus Regeneration. *Acta Biomater* **2016**, *43*, 314–326. https://doi.org/10.1016/j.actbio.2016.07.050.

(44)   Lee, C. H.; Cook, J. L.; Mendelson, A.; Moioli, E. K.; Yao, H.; Mao, J. J. Regeneration of the Articular Surface of the Rabbit Synovial Joint by Cell Homing: A Proof of Concept Study. *Lancet* **2010**, *376* (9739), 440–448. https://doi.org/10.1016/S0140-6736(10)60668-X.

(45)   Lovmand, J.; Justesen, J.; Foss, M.; Lauridsen, R. H.; Lovmand, M.; Modin, C.; Besenbacher, F.; Pedersen, F. S.; Duch, M. The Use of Combinatorial Topographical Libraries for the Screening of Enhanced Osteogenic Expression and Mineralization. *Biomaterials* **2009**, *30* (11), 2015–2022. https://doi.org/10.1016/J.BIOMATERIALS.2008.12.081.

(46)   Dalby, M. J.; Gadegaard, N.; Curtis, A. S.; Oreffo, R. O. Nanotopographical Control of Human Osteoprogenitor Differentiation. *Curr Stem Cell Res Ther* **2007**, *2* (2), 129–138. https://doi.org/10.2174/157488807780599220.

(47)   Sliogeryte, K.; Thorpe, S. D.; Lee, D. A.; Botto, L.; Knight, M. M. Stem Cell Differentiation Increases Membrane-Actin Adhesion Regulating Cell Blebability, Migration and Mechanics. *Sci Rep* **2014**, *4* (1), 7307. https://doi.org/10.1038/srep07307.

(48)   Collart-Dutilleul, P.-Y.; Panayotov, I.; Secret, E.; Cunin, F.; Gergely, C.; Cuisinier, F.; Martin, M. Initial Stem Cell Adhesion on Porous Silicon Surface: Molecular Architecture of Actin Cytoskeleton and Filopodial Growth. *Nanoscale Res Lett* **2014**, *9*, 1–10. https://doi.org/10.1186/1556-276X-9-564.

(49)   Schvartzman, M.; Palma, M.; Sable, J.; Abramson, J.; Hu, X.; Sheetz, M. P.; Wind, S. J. Nanolithographic Control of the Spatial Organization of Cellular Adhesion Receptors at the Single-Molecule Level. *Nano Lett* **2011**, *11* (3), 1306–1312.

https://doi.org/10.1021/nl104378f.

(50)   Lehnert, D.; Wehrle-Haller, B.; David, C.; Weiland, U.; Ballestrem, C.; Imhof, B. A.; Bastmeyer, M. Cell Behaviour on Micropatterned Substrata: Limits of Extracellular Matrix Geometry for Spreading and Adhesion. *J Cell Sci* **2004**, *117* (Pt 1), 41–52. https://doi.org/10.1242/jcs.00836.

(51)   Chen, C. S.; Alonso, J. L.; Ostuni, E.; Whitesides, G. M.; Ingber, D. E. Cell Shape Provides Global Control of Focal Adhesion Assembly. *Biochem Biophys Res Commun* **2003**, *307* (2), 355–361. https://doi.org/10.1016/S0006-291X(03)01165-3.

(52)   McBeath, R.; Pirone, D. M.; Nelson, C. M.; Bhadriraju, K.; Chen, C. S. Cell Shape, Cytoskeletal Tension, and RhoA Regulate Stem Cell Lineage Commitment. *Dev Cell* **2004**, *6* (4), 483–495. https://doi.org/10.1016/S1534-5807(04)00075-9.

(53)   Pablo Rodríguez, J.; González, M.; Ríos, S.; Cambiazo, V. Cytoskeletal Organization of Human Mesenchymal Stem Cells (MSC) Changes during Their Osteogenic Differentiation. *J Cell Biochem* **2004**, *93* (4), 721–731. https://doi.org/10.1002/jcb.20234.

(54)   Lu, Z.; Doulabi, B. Z.; Huang, C.; Bank, R. A.; Helder, M. N. Collagen Type II Enhances Chondrogenesis in Adipose Tissue–Derived Stem Cells by Affecting Cell Shape. *Tissue Eng Part A* **2010**, *16* (1), 81–90. https://doi.org/10.1089/ten.tea.2009.0222.

(55)   Archer, C. W.; Rooney, P.; Wolpert, L. Cell Shape and Cartilage Differentiation of Early Chick Limb Bud Cells in Culture. *Cell Differ* **1982**, *11* (4), 245–251. https://doi.org/10.1016/0045-6039(82)90072-0.

(56)   Connelly, J. T.; García, A. J.; Levenston, M. E. Interactions between Integrin Ligand

Density and Cytoskeletal Integrity Regulate BMSC Chondrogenesis. *J Cell Physiol* **2008**, *217* (1), 145–154. https://doi.org/10.1002/jcp.21484.

(57) Lee, S. J.; Yang, S. Substrate Curvature Restricts Spreading and Induces Differentiation of Human Mesenchymal Stem Cells. *Biotechnol J* **2017**, *12* (9), 1700360. https://doi.org/10.1002/biot.201700360.

BRIEFS

Bio-instructive scaffolds with controllable topographies that can guide stem cell differentiation are desirable for tissue regeneration. However, incorporation of controlled topographies to 3D printed porous scaffolds is difficult. A method is developed to directly 3D print polymer scaffolds with micro- and nano-scale pores on the strut surface. These pores show profound effects on stem cell adhesion, morphology and differentiation.

SYNOPSIS

Vortex generates small bubbles

3D printing of an vortexed viscous PCL/DCM solution

DCM evaporation

Bubbles move towards the air-solvent interface resulting in the porous surface

Non-vortex

Vortex 3200 rpm

Cell morphology and actin organisation

Porous strut

Smooth strut

Chondrogenic differentiation